CHINESE OPTICS LETTERS

Vol. 20, No. 12 | December 2022

Fabrication, testing, and assembly of high-finesse optical fiber microcavity for molecule cavity QED experiment

Yuhao Pan (潘宇豪)[1,2], Li Li (李 黎)[1,2], Xiaolong Zhou (周小龙)[1,2], Dongyu Huang (黄冬郁)[1,2], Zemin Shen (沈泽民)[1,2], Jian Wang (王 健)[1,2*], Chuanfeng Li (李传锋)[1,2], and Guangcan Guo (郭光灿)[1,2]

[1] CAS Key Laboratory of Quantum Information, University of Science and Technology of China, Hefei 230026, China

[2] CAS Center for Excellence in Quantum Information and Quantum Physics, University of Science and Technology of China, Hefei 230026, China

*Corresponding author: jwang28@ustc.edu.cn

Received April 26, 2022 | Accepted June 27, 2022 | Posted Online August 15, 2022

The ultracold molecule is a promising candidate for versatile quantum tasks due to its long-range interaction and rich internal rovibrational states. With the help of the cavity quantum electrodynamics (QED) effects, an optical cavity can be employed to increase the efficiency of the formation of the photoassociated molecules and offers a non-demolition detection of the internal states of molecules. Here, we demonstrate the production of the high-finesse optical fiber microcavity for the Rb_2 molecule cavity QED experiment, which includes the fabrication of fiber-based cavity mirrors, testing, and the assembly of ultra-high vacuum-compatible optical fiber microcavity. The optical fiber microcavity offers high cooperativity between cavity mode and ultracold molecule and paves the way for the study of molecule cavity QED experimental research.

Keywords: optical fiber microcavity; ultracold molecule; molecule cavity quantum electrodynamics.
DOI: 10.3788/COL202220.122702

1. Introduction

In ultracold molecules, complex rovibrational energy levels enrich the spectrum from microwave to visible light, and the large permanent dipole moment empowers strong intermolecular interaction[1,2], making the ultracold molecule a new form of quantum matter for quantum chemistry[3–5], quantum simulation[6,7], quantum computation[8,9], and quantum precision measurement[10–12]. To prepare molecules for the ultracold regime, two ways of producing ultracold molecules have been developed: direct cooling with special molecule species like SrF and CaF[13–17] and association from the pre-cooled atoms. In association with pre-cooled atoms, the constituent atoms are usually chosen to be easily cooled to the quantum degeneracy regime and are associated by photoassociation[18], Feshbach resonance combined with stimulated Raman adiabatic passage (STRAP)[19–21], spin-motional coupling[22], and optical Raman transition in optical tweezers[23]. Cavity quantum electrodynamics (QED) concentrates on the study of the interaction between light and matter, which plays a significant role in single-photon generation[24,25], quantum network[26], and quantum computation[27]. By tailoring the spatial boundary condition, the optical cavity enhances the resonant transition of interacting matter (called the Purcell effect) and even induces the strong coupling between cavity mode and matter forming dressed states if the coupling strength overcomes the dissipation strength. In molecule cavity QED experimental research, the optical cavity enhances the resonant energy transitions and suppresses other off-resonant transitions of complex rovibrational energy levels, which can form a near-closed optical cycle for manipulation and fluorescence detection of polyatomic molecules[28]. It can also greatly increase the production efficiency of photoassociated molecules and narrows the final state distribution to the desired state[29–31]. With the help of the strong coupling of cavity mode and molecules, the optical cavity offers a non-demolition detection of the internal state of molecules without destructively converting associated molecules to the constituent atoms or molecular ions for detection[32]. Besides, the strong coupling effect will modify the photochemical and photophysical processes in molecules, empowering the research of cavity-controlled chemistry[33,34].

The optical fiber Fabry–Pérot microcavity featuring small mode volume and high finesse is a good candidate for ultracold molecules experimental research requiring large system cooperativity[35,36]. Different from single atoms, the coupling strength of the cavity mode and molecules will be additionally reduced by the finite wavefunction overlap between the excited bound state and the ground molecular state described by $g = g_{\max}\sqrt{f_{\mathrm{FC}}}$, and then the cooperativity is $C = C_{\max} f_{\mathrm{FC}}$, where f_{FC} is the Franck–Condon factor of the transition[29]. To achieve large cooperativity ($C_{\max} \sim \mathrm{Finesse}/\omega^2$), a small waist of cavity mode and high

finesse are needed for designing an optical Fabry–Pérot cavity. Better than the super-polished bulk cavity mirror, the optical fiber cavity mirror fabricated by laser ablation has advantages in terms of smaller radius of curvature and low-roughness surface, resulting in a smaller waist and high finesse of the optical cavity after coating. The inherent optical fiber directly connected with the optical fiber microcavity eases the mode matching and collection of the intracavity photons without complex spatial optics in the bulk Fabry–Pérot cavity. Thanks to the Fabry–Pérot cavity structure, the cavity mode of optical fiber microcavity can easily be tuned to match the desired rovibrational states of ultracold molecules by varying the cavity length. The open-access of the optical fiber microcavity also facilitates the loading of molecules to the cavity mode and the sending of manipulating lasers to intracavity molecules. Compared with other types of optical resonators, the optical fiber microcavity has a narrower linewidth than the photonic crystal cavity[37,38] and a smaller mode volume than the whispering-gallery-mode cavity[39]. For molecules, the Rb_2 molecules have been exploited by researchers, which have an optical transition at 744 nm with a relatively large Franck–Condon factor of 0.37 and are easily created by photoassociation[40]. Here, we demonstrate an optical fiber Fabry–Pérot microcavity with a high finesse of 24,000 for the Rb_2 molecules, indicating that the cooperativity is expected to be about $C = C_{\max} f_{\mathrm{FC}} \approx 18$. The fiber cavity mirrors for the high-finesse optical fiber microcavity are fabricated by a homemade CO_2 laser ablation system and tested to be suitable for Rb_2 molecules at the 744 nm transition. The method of assembling an ultra-vacuum-compatible optical fiber microcavity from fiber cavity mirrors is presented. The microcavity is tested monthly in an ultra-high vacuum chamber without finesse degradation happening in other groups, which can be integrated with the ultracold molecules experimental system.

2. Experiment and Results

2.1. Fabrication of fiber cavity mirrors

Fabrication of the fiber cavity mirrors plays a central role in producing a high-finesse optical cavity, which directly determines the surface profile of cavity mirrors and optical properties. Among the various fabrication methods[41], laser ablation can polish the surface of the cavity mirror with the roughness of sub-nanometers and can cover a wide radius of curvature (ROC) range of concave mirrors from tens of micrometers to thousands of micrometers. As Fig. 1 shows, our homemade fiber mirrors fabrication system mainly consists of a CO_2 laser ablation system and a white-light-interferometer-based surface profiler. For the laser ablation system, the ablating laser pulses are obtained from an industrial continuous-wave CO_2 laser (Synrad firestar v40) chopped externally by an optical shutter. The power stability of the CO_2 laser will affect the repeatability of the fabrication, so a power meter is placed at the output of the CO_2 laser to monitor the power drift. So, varying the power of the CO_2 laser and the opening duration of the optical shutter can change the

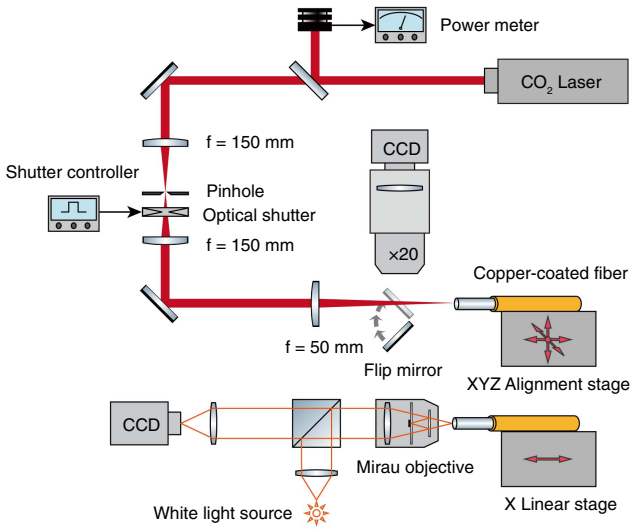

Fig. 1. Experimental setup of CO_2 laser ablation system and surface profiler for the fabrication of fiber cavity mirrors.

heating energy deposited on the tip of the optical fibers, which is one of the important factors affecting mirror features such as ROC and the diameter of the concave mirrors. To guarantee that the laser power distribution has cylindrical symmetry along the propagation direction, we apply a spatial filter with a precision pinhole at the focus of the lens to get a circular Gaussian beam. Then, the laser beam is focused to a beam waist of 50 μm by a ZnSe lens with a focal length of 50 mm. The cleaved fiber is placed on a three-dimensional alignment stage to match the tip with the focused laser beam. As a reference, the microscope combined with a flip mirror is used to locate the fiber tip and monitor the concave cavity mirror after ablation. For the surface profiler, it is convenient to fast measure the key characters of fiber mirrors in real time after ablation compared to atomic force microscopy. The central component of the surface profiler is a Mirau objective, which inherently is an interferometer comparing the optical path difference between the fiber tip path and the reference path. The white light source with a limited coherence length offers an additional envelope on the interference pattern to precisely determine the zero optical path difference. The one-axis linear stage with a positioning resolution of sub-nanometers will drive the fiber mirror moving along beam path, and then the interference patterns of the whole mirror profile can be recorded by the CCD camera. By fitting the interference patterns of each pixel, it only takes seconds for the three-dimensional profile to be constructed to characterize the fiber mirrors.

2.2. Testing of fiber cavity mirrors

The contour plot describing the fabricated fiber cavity mirror is shown in Fig. 2(a) derived from our surface profiler, which is a near-spherical concave surface. To compare our laser-ablated cavity mirror with the ideal spherical Fabry–Pérot cavity mirror, we fit the central cross section of the fiber cavity mirror with a circle equation in Fig. 2(b). Then, the difference between the data

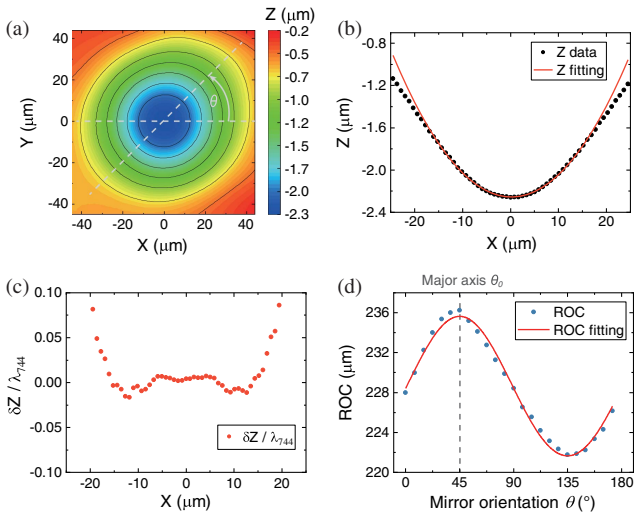

Fig. 2. (a) Contour plot of the concave fiber cavity mirror. The horizontal gray dashed line is the baseline of the mirror orientation ($\theta = 0°$), and the θ stands for the relative angle of different mirror orientations for cross sections around the mirror center. (b) Cross section of the concave fiber cavity mirror fitted by a circular equation. (c) Difference between the measured Z data and the fitting Z data on the scale of the 744 nm working wavelength. (d) The distribution of ROC for mirror orientations fitted by an ellipsoid model, and the θ_0 stands for the relative angle of the mirror orientation at the major axis.

and fitting function is derived in Fig. 2(c). The effective diameter of the fiber cavity mirror is defined as the range where the difference is below a tenth of the 744 nm working wavelength, so our fiber cavity mirror is about 40 μm in diameter. In the high-finesse optical fiber microcavity, the frequency splitting of different polarizations is sensitive to the eccentricity of the elliptical cavity mirrors, which should be minimized for a polarization-degenerate cavity. The differential phase shift between the two polarization eigenmodes from one elliptical cavity mirror is[42,43]

$$\Delta\varphi = \frac{1}{k}\frac{R_1 - R_2}{R_1 R_2}, \tag{1}$$

where $k = 2\pi/\lambda$ is the wavevector, and R_1 and R_2 are the ROCs at the major and minor axes of the elliptical mirror surface, respectively. For the optical cavity constructed by the two elliptical cavity mirrors, the total differential phase shift acquired from the round trip in the cavity is[42,43]

$$\Delta\varphi_{\text{total}} = \sqrt{\Delta\varphi_1^2 + \Delta\varphi_2^2 + 2\Delta\varphi_1\Delta\varphi_2\cos(2\delta)}, \tag{2}$$

where φ_1 and φ_2 are the differential phase shifts contributed by the two elliptical cavity mirrors, respectively; δ is the relative angle between the major axes of the two elliptical cavity mirrors. So, by adjusting the relative angle δ, the total differential phase shift can be reduced to a minimum value of $|\Delta\varphi_1 - \Delta\varphi_2|$. The frequency splitting of different polarizations is[42,43]

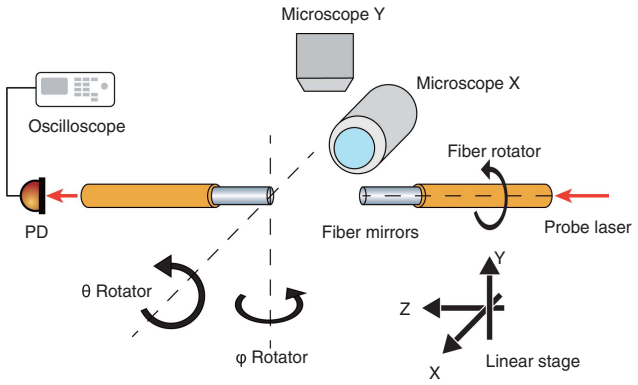

Fig. 3. Experimental setup of the high-precision alignment testing platform.

$$\Delta\upsilon = \frac{\upsilon_{\text{FSR}}}{2\pi}\Delta\varphi_{\text{total}}, \tag{3}$$

where υ_{FSR} is the free spectral range of the cavity. From the contour plot of each cavity mirror, as shown in Fig. 2(a), the ROC at the major and minor axes can be found by scanning the different orientations and fitting the measured data around the mirror center. The distribution of ROC for the different orientations is shown in Fig. 2(d) and is fitted by an ellipsoid model whose distribution can be described by the equation

$$\text{ROC}(\theta) = \frac{1}{\cos^2(\theta - \theta_0)/R_1 + \sin^2(\theta - \theta_0)/R_2}, \tag{4}$$

where θ is the mirror orientation of the cross section, and θ_0 is the orientation at the major axis of the elliptical cavity mirror. From Fig. 2(d), the ROCs at the major and minor axes are 236 μm and 222 μm, respectively. Combined with the other fiber mirror with the ROCs of 249 μm and 238 μm at the major and minor axes, the minimum theoretical total differential phase shift is about 9.6 μrad. Then, the polarization degeneracy can be maintained with a limited finesse of about 330,000 theoretically, considering that the frequency splitting is half of the cavity linewidth. Even combined with a plane mirror, the limited finesse keeping the degeneracy will be about 100,000. So, the small eccentricity of our fiber cavity mirror results in an indistinguishable frequency splitting, so our fiber cavity mirror shows the ability to make a high-finesse polarization-degenerate cavity. The main reason for the eccentricity is that our fiber cleaver causes defects at the fringe of the fiber tip, making an asymmetrical and uneven plane.

Coated with the highly reflective coating at the multiwavelengths of 744 nm, 780 nm, and 850 nm, the optical properties of the fabricated fiber cavity mirrors need to be tested in a form of a Fabry–Pérot cavity with the help of a high-precision alignment testing platform. As Fig. 3 shows, our testing platform has six degrees of freedom to control the relative position and orientation between the two fiber cavity mirrors forming the optical cavity. The fiber cavity mirror in the right can travel in the three-dimensional direction driven by three one-axis linear stages and can oscillate fast along the optical cavity axis in

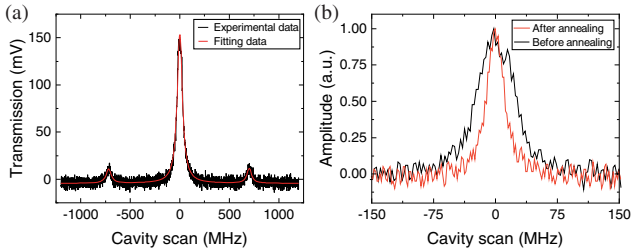

Fig. 4. (a) Transmission signal of optical fiber microcavity at the 744 nm working wavelength with the cavity length of 100 μm. (b) Transmission peaks of optical fiber microcavity consisting of two low-transmission (LT) cavity mirrors before annealing (black line) and after annealing (red line).

several micrometers actuated by a piezo to scan the cavity length for a transmission signal. The fiber rotator can rotate the relative angle between the major axes of the two elliptical cavity mirrors in the right to suppress the frequency splitting of different polarizations[42,43]. For the fiber cavity mirror in the left, the position is kept still, but the orientation can be rotated in the two orthogonal directions. The two microscopes are placed in the vertical and horizontal directions for the coarse alignment of the two fiber cavity mirrors and cavity length measurement. A probe laser is sent into the right fiber cavity mirror, and the transmission signal is detected at the output of the left fiber cavity mirror and is displayed on the oscilloscope. Optimizing the transmission signal by finely adjusting the position and orientation of the two fiber cavity mirrors can reach the best mode-matching efficiency between the optical fiber mode and cavity mode[44]. As Fig. 4(a) shows, the transmission peak of the optical fiber microcavity at the 744 nm working wavelength is recorded, and the full-width at half-maximum (FWHM) is measured to be about 62 MHz by comparing it with the two 710 MHz electro-optic modulator (EOM)-generated sidebands. With the cavity length of 100 μm measured by the microscope, the finesse at 744 nm is Finesse = FSR/FWHM ≈ 24,000.

After basic testing, annealing is applied to the two fiber cavity mirrors to increase the finesse of the optical cavity, which proves to be an effective way of reducing the absorption loss of Ta_2O_5 layers in multilayer dielectric coatings made by ion beam sputtering (IBS)[45,46]. We perform the annealing of the fiber mirrors in our homemade oven, which can be heated to a maximum temperature of 450°C. In the annealing process, the temperature is increased gradually in a step of 50°C per 5 min and is kept at 400°C for 4 h. To illustrate the performance of annealing, we compare the finesse of the optical cavity at the fixed cavity lengths, which represents the change of the intracavity loss. In Table 1, the first testing optical cavity comprising the relatively high-transmission (HT, $T_1 = 130$ ppm) and low-transmission (LT, $T_2 = 13$ ppm) fiber cavity mirrors stands for the typical configuration of our optical fiber microcavity. To make the annealing effect apparent, two LT ($T = 13$ ppm) fiber cavity mirrors are used to compose the second testing optical cavity, where the absorption and scattering losses of the coatings account for the main part of the intracavity loss. As a result, the finesse of the first testing optical cavity is increased from

Table 1. The Finesse of Two Optical Fiber Microcavities before and after Annealing[a].

	Before Annealing		After Annealing	
Types	$L = 50$ μm	$L = 100$ μm	$L = 50$ μm	$L = 100$ μm
HT + LT	37,120	31,175	41,328	40,543
LT + LT	60,735	69,785	112,166	111,080

[a]The first optical fiber microcavity consists of a high-transmission (HT) cavity mirror and a low-transmission (LT) cavity mirror. Both cavity mirrors in the second optical fiber microcavity are LT.

about 30,000 to 40,000, indicating the loss reduction of about 23 ppm, and the second testing optical cavity also has a loss reduction of about 17 ppm, which proves that annealing is an efficient way of improving optical properties of IBS coatings for the high-finesse optical cavity. As Fig. 4(b) shows, the narrowing of the transmission peak from 50 MHz (FWHM) to 27 MHz (FWHM) after annealing for the optical fiber cavity comprising two LT cavity mirrors at 50 μm illustrates directly the reduction of intracavity loss.

2.3. Assembly of optical fiber microcavity

For coupling to the Rb_2 molecules, the whole optical fiber microcavity will be placed in an ultra-high vacuum chamber. Although some complicated configurations are using vacuum-compatible multi-dimensional linear stages to finely align fiber cavity mirrors in the vacuum chamber[26,46], we apply an economical, simple, and stable configuration of assembling optical cavities by gluing the fiber cavity mirrors to a whole. As Fig. 5(a) shows, each side of the fiber cavity mirror is glued in the glass V groove. Below the V groove, a shear piezo with a large resonance frequency is employed to drive the cavity mirror along the cavity axis for cavity length stabilization or resonance frequency tuning. For the stable connection of the shear piezo, high-temperature-curing glue is applied on the contact surfaces of

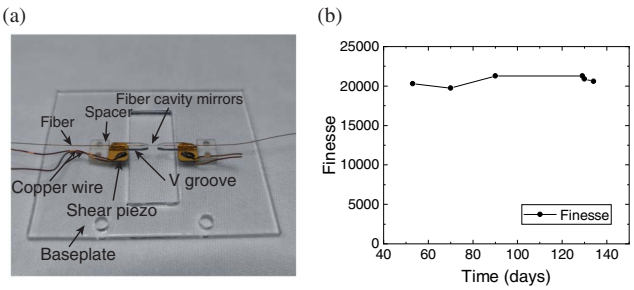

Fig. 5. (a) Assembly of the optical fiber microcavity consists of fiber cavity mirrors, V grooves, piezos, copper wires, spacers, and the baseplate. (b) Finesse change of the optical fiber microcavity tested in the ultra-high vacuum chamber at the 850 nm locking wavelength for 4 months. The fluctuation of the measured finesse results from the uncertainty of the measurement method.

the V groove and the spacer. The vacuum-compatible copper wires offering the external control voltage for the shear piezo are glued on each side of the piezo plate by a silver-filled conductive glue for a reliable electric connection. The spacer is made of machinable ceramic and has two screw holes for the connection to the high-precision alignment testing platform. After fine adjustment with the help of precise alignment stages, the fiber mirrors forming the optimized optical Fabry–Pérot cavity are kept still on the stages, and the spacers of them are glued on the glass baseplate to assemble the optical cavity by the UV-curing glue for fast curing without slow position drift of cavity mirrors. All the components and glues used in our optical cavity assembly are tested to be ultra-high vacuum-compatible.

Some researchers report the finesse degradation of high-finesse optical fiber microcavity in ultra-high vacuum for UV wavelength[47] and near-infrared (NIR) wavelength[48]. So, we test our optical fiber microcavity assembly in an ultra-high vacuum chamber ($< 10^{-9}$ mbar) for months. By recording the finesse at the 850 nm locking wavelength, the finesse degradation is not observed in our high-finesse optical fiber microcavity, as shown in Fig. 5(b). The finesse of our optical fiber microcavity at 850 nm is kept around 20,000, proving that the optical fiber microcavity assembly is compatible with the ultra-high vacuum environment.

3. Conclusion

In this Letter, we illustrate the fabrication of fiber cavity mirrors by the CO_2 laser ablation system and characterize the mirrors by the homemade surface profiler. The testing of the aligned fiber cavity mirrors on the high-precision alignment testing platform shows the ability to form the high-finesse optical fiber microcavity for Rb_2 energy level transition at 744 nm. We also observe the increase of cavity finesse after the annealing process due to the decrease of absorption loss on the cavity mirrors, which can be widely used in the application of optical fiber cavities. The assembly of the optical fiber microcavity is vacuum compatible without finesse degradation, and the cavity length can be tuned by the shear piezo, which is suitable for the ultracold molecule experimental research. Our optical fiber microcavity will be helpful to the study of molecule cavity QED and will play an important role in molecule formation by controlling the ultracold chemistry process.

Acknowledgement

This work was supported by the National Key Research and Development Program of China (No. 2017YFA0304100), National Natural Science Foundation of China (Nos. 11804330 and 11821404), and the Fundamental Research Funds for the Central Universities.

References

1. J. L. Bohn, A. M. Rey, and J. Ye, "Cold molecules: progress in quantum engineering of chemistry and quantum matter," Science **357**, 1002 (2017).
2. S. A. Moses, J. P. Covey, M. T. Miecnikowski, D. S. Jin, and J. Ye, "New frontiers for quantum gases of polar molecules," Nat. Phys. **13**, 13 (2017).
3. Y. Liu, M.-G. Hu, M. A. Nichols, D. Yang, D. Xie, H. Guo, and K.-K. Ni, "Precision test of statistical dynamics with state-to-state ultracold chemistry," Nature **593**, 379 (2021).
4. W. G. Tobias, K. Matsuda, J.-R. Li, C. Miller, A. N. Carroll, T. Bilitewski, A. M. Rey, and J. Ye, "Reactions between layer-resolved molecules mediated by dipolar spin exchange," Science **375**, 1299 (2022).
5. H. Yang, X.-Y. Wang, Z. Su, J. Cao, D.-C. Zhang, J. Rui, B. Zhao, C.-L. Bai, and J.-W. Pan, "Evidence for the association of triatomic molecules in ultracold $^{23}Na^{40}K + {}^{40}K$ mixtures," Nature **602**, 229 (2022).
6. H. Weimer, "Quantum simulation of many-body spin interactions with ultracold polar molecules," Mol. Phys. **111**, 1753 (2013).
7. T. Schuster, F. Flicker, M. Li, S. Kotochigova, J. E. Moore, J. Ye, and N. Y. Yao, "Floquet engineering ultracold polar molecules to simulate topological insulators," Phys. Rev. A **103**, 063322 (2021).
8. P. Yu, L. W. Cheuk, I. Kozyryev, and J. M. Doyle, "A scalable quantum computing platform using symmetric-top molecules," New J. Phys. **21**, 093049 (2019).
9. S. F. Yelin, K. Kirby, and R. Côté, "Schemes for robust quantum computation with polar molecules," Phys. Rev. A **74**, 050301 (2006).
10. V. Andreev, D. G. Ang, D. DeMille, J. M. Doyle, G. Gabrielse, J. Haefner, N. R. Hutzler, Z. Lasner, C. Meisenhelder, B. R. O'Leary, C. D. Panda, A. D. West, E. P. West, X. Wu, and A. Collaboration, "Improved limit on the electric dipole moment of the electron," Nature **562**, 355 (2018).
11. T. Bilitewski, L. De Marco, J.-R. Li, K. Matsuda, W. G. Tobias, G. Valtolina, J. Ye, and A. M. Rey, "Dynamical generation of spin squeezing in ultracold dipolar molecules," Phys. Rev. Lett. **126**, 113401 (2021).
12. B. L. Augenbraun, Z. D. Lasner, A. Frenett, H. Sawaoka, C. Miller, T. C. Steimle, and J. M. Doyle, "Laser-cooled polyatomic molecules for improved electron electric dipole moment searches," New J. Phys. **22**, 022003 (2020).
13. E. B. Norrgard, D. J. McCarron, M. H. Steinecker, M. R. Tarbutt, and D. DeMille, "Submillikelvin dipolar molecules in a radio-frequency magneto-optical trap," Phys. Rev. Lett. **116**, 063004 (2016).
14. S. Ding, Y. Wu, I. A. Finneran, J. J. Burau, and J. Ye, "Sub-Doppler cooling and compressed trapping of YO molecules at μK temperatures," Phys. Rev. X **10**, 021049 (2020).
15. L. Anderegg, B. L. Augenbraun, E. Chae, B. Hemmerling, N. R. Hutzler, A. Ravi, A. Collopy, J. Ye, W. Ketterle, and J. M. Doyle, "Radio frequency magneto-optical trapping of CaF with high density," Phys. Rev. Lett. **119**, 103201 (2017).
16. L. Anderegg, L. W. Cheuk, Y. Bao, S. Burchesky, W. Ketterle, K.-K. Ni, and J. M. Doyle, "An optical tweezer array of ultracold molecules," Science **365**, 1156 (2019).
17. Y. Wu, J. J. Burau, K. Mehling, J. Ye, and S. Ding, "High phase-space density of laser-cooled molecules in an optical lattice," Phys. Rev. Lett. **127**, 263201 (2021).
18. K. M. Jones, E. Tiesinga, P. D. Lett, and P. S. Julienne, "Ultracold photoassociation spectroscopy: long-range molecules and atomic scattering," Rev. Mod. Phys. **78**, 483 (2006).
19. C. Chin, R. Grimm, P. Julienne, and E. Tiesinga, "Feshbach resonances in ultracold gases," Rev. Mod. Phys. **82**, 1225 (2010).
20. K. Bergmann, H.-C. Nägerl, C. Panda, G. Gabrielse, E. Miloglyadov, M. Quack, G. Seyfang, G. Wichmann, S. Ospelkaus, A. Kuhn, S. Longhi, A. Szameit, P. Pirro, B. Hillebrands, X.-F. Zhu, J. Zhu, M. Drewsen, W. K. Hensinger, S. Weidt, T. Halfmann, H.-L. Wang, G. S. Paraoanu, N. V. Vitanov, J. Mompart, T. Busch, T. J. Barnum, D. D. Grimes, R. W. Field, M. G. Raizen, E. Narevicius, M. Auzinsh, D. Budker, A. Pálffy, and C. H. Keitel, "Roadmap on STIRAP applications," J. Phys. B **52**, 202001 (2019).
21. L. D. Marco, G. Valtolina, K. Matsuda, W. G. Tobias, J. P. Covey, and J. Ye, "A degenerate Fermi gas of polar molecules," Science **363**, 853 (2019).
22. X. He, K. Wang, J. Zhuang, P. Xu, X. Gao, R. Guo, C. Sheng, M. Liu, J. Wang, J. Li, G. V. Shlyapnikov, and M. Zhan, "Coherently forming a single molecule in an optical trap," Science **370**, 331 (2020).
23. Y. Yu, K. Wang, J. D. Hood, L. R. B. Picard, J. T. Zhang, W. B. Cairncross, J. M. Hutson, R. Gonzalez-Ferez, T. Rosenband, and K.-K. Ni, "Coherent optical creation of a single molecule," Phys. Rev. X **11**, 031061 (2021).

24. N. Tomm, A. Javadi, N. O. Antoniadis, D. Najer, M. C. Löbl, A. R. Korsch, R. Schott, S. R. Valentin, A. D. Wieck, A. Ludwig, and R. J. Warburton, "A bright and fast source of coherent single photons," Nat. Nanotechnol. **16**, 399 (2021).
25. Y. Huang, Z. Dang, X. He, and Z. Fang, "Engineering of single-photon emitters in hexagonal boron nitride [Invited]," Chin. Opt. Lett. **20**, 032701 (2022).
26. M. Brekenfeld, D. Niemietz, J. D. Christesen, and G. Rempe, "A quantum network node with crossed optical fibre cavities," Nat. Phys. **16**, 647 (2020).
27. S. Daiss, S. Langenfeld, S. Welte, E. Distante, P. Thomas, L. Hartung, O. Morin, and G. Rempe, "A quantum-logic gate between distant quantum-network modules," Science **371**, 614 (2021).
28. D. Wang, H. Kelkar, D. Martin-Cano, D. Rattenbacher, A. Shkarin, T. Utikal, S. Götzinger, and V. Sandoghdar, "Turning a molecule into a coherent two-level quantum system," Nat. Phys. **15**, 483 (2019).
29. T. Kampschulte and J. Hecker Denschlag, "Cavity-controlled formation of ultracold molecules," New J. Phys. **20**, 123015 (2018).
30. J. Pérez-Ríos, M. E. Kim, and C.-L. Hung, "Ultracold molecule assembly with photonic crystals," New J. Phys. **19**, 123035 (2017).
31. D. Wellnitz, S. Schütz, S. Whitlock, J. Schachenmayer, and G. Pupillo, "Collective dissipative molecule formation in a cavity," Phys. Rev. Lett. **125**, 193201 (2020).
32. M. Zhu, Y.-C. Wei, and C.-L. Hung, "Resonator-assisted single-molecule quantum state detection," Phys. Rev. A **102**, 023716 (2020).
33. F. Herrera and F. C. Spano, "Cavity-controlled chemistry in molecular ensembles," Phys. Rev. Lett. **116**, 238301 (2016).
34. F. J. Garcia-Vidal, C. Ciuti, and T. W. Ebbesen, "Manipulating matter by strong coupling to vacuum fields," Science **373**, eabd0336 (2021).
35. D. Hunger, T. Steinmetz, Y. Colombe, C. Deutsch, T. W. Hänsch, and J. Reichel, "A fiber Fabry-Perot cavity with high finesse," New J. Phys. **12**, 065038 (2010).
36. H. Pfeifer, L. Ratschbacher, J. Gallego, C. Saavedra, A. Faßbender, A. von Haaren, W. Alt, S. Hofferberth, M. Köhl, S. Linden, and D. Meschede, "Achievements and perspectives of optical fiber Fabry-Perot cavities," Appl. Phys. B **128**, 29 (2022).
37. L. Zhou, C. Wang, A. Yi, C. Shen, Y. Zhu, K. Huang, M. Zhou, J. Zhang, and X. Ou, "Photonic crystal nanobeam cavities based on 4H-silicon carbide on insulator," Chin. Opt. Lett. **20**, 031302 (2022).
38. L. Fang, X. Gan, and J. Zhao, "High-*Q* factor photonic crystal cavities with cut air holes [Invited]," Chin. Opt. Lett. **18**, 111402 (2020).
39. S. Subramanian, S. Vincent, and F. Vollmer, "Effective linewidth shifts in single-molecule detection using optical whispering gallery modes," Appl. Phys. Lett. **117**, 151106 (2020).
40. M. A. Bellos, D. Rahmlow, R. Carollo, J. Banerjee, O. Dulieu, A. Gerdes, E. E. Eyler, P. L. Gould, and W. C. Stwalley, "Formation of ultracold Rb_2 molecules in the $v'' = 0$ level of the $a^3\Sigma_u^+$ state via blue-detuned photoassociation to the $1^3\pi_g$ state," Phys. Chem. Chem. Phys. **13**, 18880 (2011).
41. M. H. Bitarafan and R. G. DeCorby, "On-chip high-finesse Fabry-Perot microcavities for optical sensing and quantum information," Sensors **17**, 1748 (2017).
42. M. Uphoff, M. Brekenfeld, G. Rempe, and S. Ritter, "Frequency splitting of polarization eigenmodes in microscopic Fabry-Perot cavities," New J. Phys. **17**, 013053 (2015).
43. J.-M. Cui, K. Zhou, M.-S. Zhao, M.-Z. Ai, C.-K. Hu, Q. Li, B.-H. Liu, J.-L. Peng, Y.-F. Huang, C.-F. Li, and G.-C. Guo, "Polarization nondegenerate fiber Fabry-Perot cavities with large tunable splittings," Appl. Phys. Lett. **112**, 171105 (2018).
44. J. Gallego, S. Ghosh, S. K. Alavi, W. Alt, M. Martinez-Dorantes, D. Meschede, and L. Ratschbacher, "High-finesse fiber Fabry-Perot cavities: stabilization and mode matching analysis," Appl. Phys. B **122**, 47 (2016).
45. Y. Zhao, Y. Wang, H. Gong, J. Shao, and Z. Fan, "Annealing effects on structure and laser-induced damage threshold of Ta_2O_5/SiO_2 dielectric mirrors," Appl. Surf. Sci. **210**, 353 (2003).
46. B. Brandstätter, A. McClung, K. Schüppert, B. Casabone, K. Friebe, A. Stute, P. O. Schmidt, C. Deutsch, J. Reichel, R. Blatt, and T. E. Northup, "Integrated fiber-mirror ion trap for strong ion-cavity coupling," Rev. Sci. Instrum. **84**, 123104 (2013).
47. D. Gangloff, M. Shi, T. Wu, A. Bylinskii, B. Braverman, M. Gutierrez, R. Nichols, J. Li, K. Aichholz, M. Cetina, L. Karpa, B. Jelenković, I. Chuang, and V. Vuletić, "Preventing and reversing vacuum-induced optical losses in high-finesse tantalum (V) oxide mirror coatings," Opt. Express **23**, 18014 (2015).
48. J. Gallego, W. Alt, T. Macha, M. Martinez-Dorantes, D. Pandey, and D. Meschede, "Strong purcell effect on a neutral atom trapped in an open fiber cavity," Phys. Rev. Lett. **121**, 173603 (2018).